Measurement 260 (2026) 119809

Contents lists available at ScienceDirect

Measurement

journal homepage: www.elsevier.com/locate/measurement

Voltage-based balancing technique for half printed Wheatstone bridges

Michela Borghetti *, Emilio Sardini, Mauro Serpelloni

Department of Information Engineer, University of Brescia, via Branze 38, Brescia, Italy

ARTICLE INFO

Keywords:
Bridge circuits
Resistors
Resistance
Electrical resistance measurement
Strain measurement
Resistive sensors

ABSTRACT

The Wheatstone bridge is a fundamental circuit in resistive sensing systems, widely used for converting small resistance changes into measurable voltage signals. As the demand for smart, flexible, and scalable electronic systems grows, printed electronics technologies are increasingly adopted for sensor fabrication. These techniques enable direct deposition of conductive inks on various substrates, making them ideal for applications in wearable electronics, soft robotics, and structural health monitoring. Printed strain gauges are promising due to their simplicity and compatibility with flexible substrates. However, the high resistance tolerance introduced by the printing process remains a significant challenge. Traditional solutions involve manual trimming or precision components, which are not practical for scalable and easily deployable systems. This work presents a novel measurement method designed for printed strain gauges with high resistance tolerance, applied to a practical case involving a half Wheatstone bridge. The initial resistance mismatch of the printed strain gauges is compensated by adjusting a single controllable reference voltage, eliminating the need for trimming or complex circuities. The proposed method was experimentally validated with printed strain gauges on a steel cantilever beam, achieving a linearity error of less than 5%/FS (with FS = 0.018%) and a negligible offset less than 21 μV. By compensating for the initial offset caused by resistance mismatch through the adjustment of the bridge reference voltages, the proposed method preserves signal linearity and enables an effective operation of the subsequent cascaded amplification stage, thereby enhancing the overall performance of printed sensor systems.

1. Introduction

The Wheatstone bridge (WB) is a fundamental circuit in resistive sensing systems and remains the most widely adopted method for converting small resistance changes into measurable voltage signals [1–4]. The full WB configuration offers excellent sensitivity and temperature compensation—key features in demanding sensing applications such as strain measurement [5], pressure monitoring [6], and biomechanical sensing [7]. As the demand for smart, flexible, and scalable electronic systems grows, there is growing interest in additive manufacturing technologies [8]—such as inkjet printing [9–11] and aerosol jet printing [12–14]—for sensor fabrication. These techniques enable the direct deposition of conductive or functional inks onto a wide variety of substrates, such as polymers, textiles, and even biodegradable materials [15]. Unlike conventional subtractive processes, printed electronics is additive and material-efficient, and it offers greater flexibility in both substrate choice and functional material composition. This makes it ideal for applications in wearable electronics, soft robotics, structural health monitoring, and disposable or conformal sensor platforms [16].

Among various sensing elements, printed strain gauges are particularly promising due to their simplicity, compatibility with flexible substrates, and ability to be embedded directly into mechanical structures [17]. Additionally, the variety of functional materials available for printed strain gauges allows achieving higher sensitivity. This flexibility in material choice enables the optimization of sensor performance for specific applications, enhancing the overall effectiveness of the sensing system [18]. However, one of the most critical limitations is the high resistance tolerance inherent to the printing process [19]. Variations in droplet size, substrate roughness, ink formulation, and environmental conditions can lead to a substantial mismatch between the nominally identical resistors of a Wheatstone bridge. In full-bridge configurations, such mismatch generates significant offset voltages that complicate amplification and may saturate the signal-conditioning chain. This ultimately reduces measurement accuracy [20].

Traditional solutions to this problem often involve post-fabrication trimming techniques, which can achieve tolerances below 0.02% [21], but at the cost of increased design complexity and manufacturing expenses. Another approach is the use of additional components to cancel

* Corresponding author.
E-mail address: michela.borghetti@unibs.it (M. Borghetti).

https://doi.org/10.1016/j.measurement.2025.119809
Received 10 July 2025; Received in revised form 31 October 2025; Accepted 19 November 2025
Available online 22 November 2025

the output voltage caused by the sensor and resistor tolerances. For instance, in [3], a JFET replaces a fixed resistor in a quarter-bridge configuration to null the voltage between the bridge nodes, while in [22] two sets of series–parallel resistors are connected in parallel with the WB to enable offset adjustment. However, these methods either increase circuit complexity or are not suitable for half- and full-bridge configurations. Active circuits or application-specific integrated circuits (ASICs) have also been employed to compensate for bridge imbalance [23–27]. A notable example is presented by De Marcellis et al. [25], who introduced a current-based measurement technique capable of detecting minimal resistance variations in initially unbalanced Wheatstone bridges. Their method uses external control voltages to electrically compensate for bridge mismatches, with active components such as second-generation current conveyors (CCII) and operational amplifiers in transimpedance configurations. This approach demonstrated the ability to detect resistance changes as small as 0.00008%. However, it requires a complex analog front-end, high-precision components, and careful tuning, making it less practical for printed sensor applications where simplicity and integration are essential. Despite the growing relevance of printed electronics, the literature lacks simple and scalable methods to balance half Wheatstone bridges with high-tolerance resistive sensors, without relying on trimming or expensive analog circuitry. Existing solutions could not be well-suited for printed and scalable systems, as they may increase production complexity and may require additional power or circuit overhead. In a recent study [20], a novel voltage-based balancing technique was proposed to compensate initial resistance mismatches by adjusting dual reference voltages, eliminating the bridge offset without affecting gain. That method was validated through simulations and preliminary experimental results using commercial resistors, but it was limited to full-bridge configurations. It also required measuring all four resistors to regulate the reference voltages and achieve balance. However, the half-bridge configuration is widely used in applications where increased strain-gauge sensitivity and temperature compensation are needed [28], and thus requires a simple method to address sensor tolerance. In this paper, we propose a method specifically designed for half-bridge configurations, which is easily implementable and applicable to realistic scenarios, such as printed sensors. Compared with the voltage-based balancing method proposed in [20], the present approach is optimized for half-bridge configurations and achieves more efficient compensation of printed strain-gauge tolerance with minimal instrumentation. Furthermore, the novel approach is experimentally validated on real printed sensors fabricated using aerosol jet printing by applying it on a measurement system composed of benchtop instrumentation. Specifically, we present an enhanced implementation applied to a practical case involving printed strain gauges on a flexible cantilever beam. This setup represents an example of smart object integration and demonstrates the feasibility of the proposed method in handling large tolerance spreads without post-processing or complex analog front-end design. The proposed approach, unlike traditional bridge balancing or zeroing, achieves compensation through a single controllable reference voltage, without the need for manual trimming or complex analog circuitry. This makes it highly suitable for scalable, low-cost, and flexible electronics applications. The method is straightforward to implement and can be easily adapted for automatic calibration and integration with printed circuit technologies.

2. Materials and methods

2.1. Proposed balancing method and sensor response estimation

The proposed method is designed for high-tolerance metallic strain sensors in a half WB configuration, but it can be extended for other types of sensors.

As depicted in Fig. 1, the proposed method is applied on a modified half WB configuration, where a controllable voltage reference (V_{E1}) is regulated to ensure a null output voltage (V_{out}), when the strain is zero ($x = 0$).

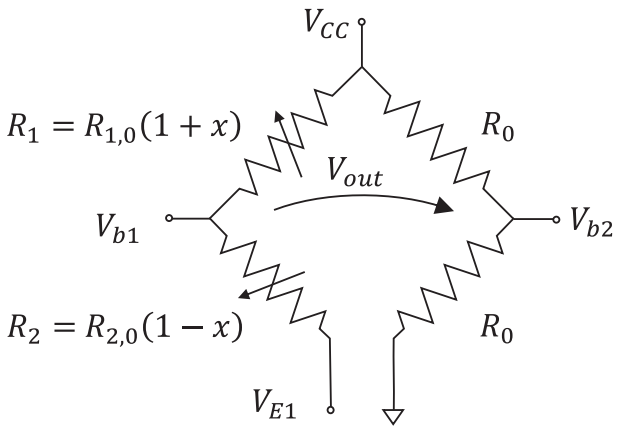

Fig. 1. Half Wheatstone bridge configuration for high-tolerance strain sensors. x is the fractional relative change in the sensor resistance related to the strain (ε), and $R_{i,0}$ (with i = 1,2) is the resistance at $\varepsilon = 0$.

As for the classical half WB, two fixed resistors – commercial resistors or dummy sensors – are chosen of value R_0 to obtain

$$V_{b2} = \frac{V_{CC}}{2} \tag{1}$$

while V_{b1} depends on the initial resistance value of two sensors (*i.e.,* null strain), $R_{1,0}$ and $R_{2,0}$, and on their relative change (x):

$$V_{b1} = \frac{V_{CC}R_{2,0}(1-x) + V_{E1}R_{1,0}(1+x)}{R_{1,0}(1+x) + R_{2,0}(1-x)} \tag{2}$$

In the case of metallic strain gauge sensors, x of the i-th sensor of the half WB is defined as the fractional change of the resistance (ΔR_i) with respect to the $R_{i,0}$, and depends on the strain (ε) as:

$$x = \frac{\Delta R_i}{R_{i,0}} = K{\cdot}\varepsilon,\ i = 1,2 \tag{3}$$

where K is the gauge factor of the strain sensor. In a WB configuration, K is supposed to be equal for all the sensors.

(2) can be simplified by defining α as the ratio of the two sensors' initial resistances, that is

$$\alpha = \frac{R_{2,0}}{R_{1,0}} \tag{4}$$

ideally, $\alpha = 1$ indicates perfect matching between the sensors, resulting in zero output voltage at zero strain. Any deviation from $\alpha = 1$ introduces an initial imbalance, causing a non-zero output voltage even in the absence of strain. The further α deviates from unity, the greater the offset voltage at rest.

In

$$V_{b1} = \frac{V_{CC}\alpha(1-x) + V_{E1}(1+x)}{(1+x) + \alpha(1-x)} \tag{5}$$

in the case of $V_{E1} = 0$ (classical half WB), the output of the bridge at $x = 0$ can be expressed as

$$V_{out,x=0 \wedge V_{E1}=V_{EE}} = V_{b2} - V_{b1} = \frac{V_{CC}(1-\alpha)}{2(1+\alpha)} \tag{6}$$

and it is null only when the two sensors have the same initial resistances ($\alpha = 1$).

The proposed method is based on regulating V_{E1} to balance the bridge when $x = 0$: $V_{out,x=0}$ is null when

$$V_{b1} = V_{b2} = V_b = \frac{V_{CC}}{2} \tag{7}$$

which is obtained when V_{E1} assumes the value V_{E1c}, defined as

$$V_{E1c} = (1-\alpha)\frac{V_{CC}}{2} \tag{8}$$

To guarantee to work within the power supplies ranges, V_{E1} is supposed to range between $-V_{CC}$ and V_{CC}. In a WB configuration, a negative power supply is usually available, since the subsequent amplification stage that requires both power supplies is usually present. It can be demonstrated that $-V_{CC} \leq V_{E1} \leq V_{CC}$ is valid until $\alpha = 3$, which corresponds to the tolerance on the resistances of 50%. Tolerances better than 50% are always expected even for sensors fabricated by emerging printing technologies, otherwise, sensors can behave dramatically differently in terms of sensitivity.

When $V_{E1} = V_{E1c}$, the output of the bridge is

$$V_{out} = x\frac{\alpha}{[(1-\alpha)x + 1 + \alpha]}V_{CC} \tag{9}$$

The output shows a linear correlation with x (Fig. 2), even for a wide range (x from –10% to +10%), which is realistic for printed metal-based strain sensors [29,30], with a R-squared value between 0.9995 and 1 according to α.

The same linear behavior is obtained for different value of V_{CC}, while the slope increases for increasing the value of V_{CC}. Indeed, since strain gauges work for small deformation (less than 2%), as demonstrated in [20], V_{out} can be approximated to $V_{out,lin}$, and thus

$$V_{out,lin} = x\frac{\alpha}{(1+\alpha)}V_{CC} \tag{10}$$

The slope of this linear approximation is:

$$m_{lin} = \frac{\alpha}{[1+\alpha]}V_{CC}, \tag{11}$$

strongly depends on the initial mismatch, as expected, and on V_{CC}—higher the V_{CC} value, higher the m value for a fixed α. As shown in Fig. 3, the slope of the least squares regression line of V_{out} (m) normalized on V_{CC} depends on the initial resistance mismatch (α from 0.4 to 1.8) and it can be considered equal to m_{lin}, simplifying the estimation of x from the measurement of V_{out}.

x can be exactly estimated from V_{out} measurement by solving (9) as a first-degree equation, and thus

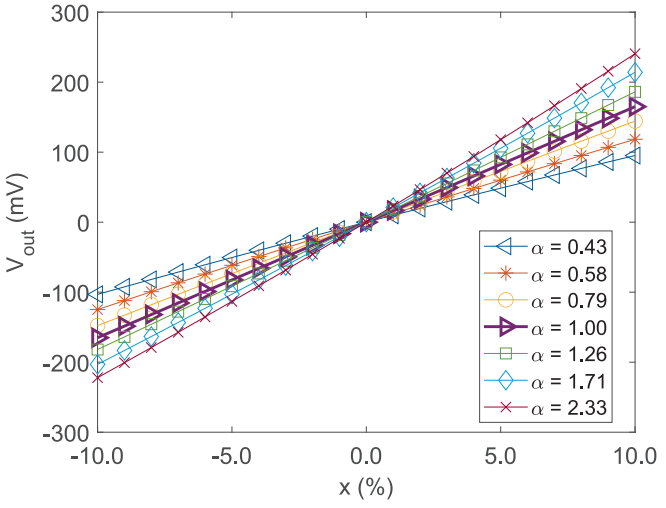

Fig. 2. Theorical WB output according to relative fractional change of the resistance x for different initial resistance mismatch α, (V_{CC} = 3.3 V).

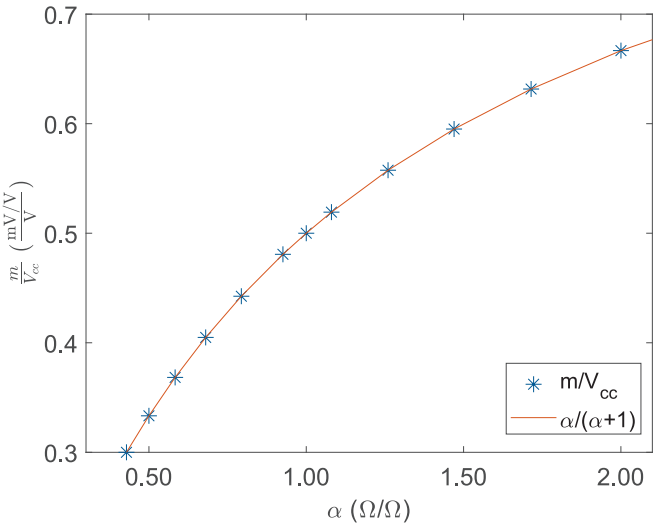

Fig. 3. Slope of the least squares regression line of V_{out} (star plot) and $V_{out,lin}$ (red line) according to α, normalized on V_{CC}. (For interpretation of the references to colour in this figure legend, the reader is referred to the web version of this article.)

$$x_{est} = \frac{(1+\alpha)V_{out}}{\alpha V_{CC} - (1-\alpha)V_{out}} \tag{12}$$

Otherwise, x can be found easily from the measurement of V_{out}, by solving (10) as

$$x_{est,lin} = \frac{(1+\alpha)}{\alpha V_{CC}}V_{out} \tag{13}$$

According to (8), the accuracy of V_{E1c} depends on the accuracy of α. An exact estimation of α and thus of V_{E1c} introduces an offset on V_{out}, which can significantly affect the measurements of small strain measurements, as in the case of the strain gauge. The two main alternatives to estimate α need benchtop instrumentation, and they are:

a) measuring $R_{1,0}$ and $R_{2,0}$ with a benchtop multimeter and calculating α by using (4);

b) measuring V_{b1} with a benchtop instrument and calculating α.

These two methods could not be viable when further calibrations are required during operation. An alternative method, used in this work, consists of the regulation of V_{E1c} until V_{out} reaches 0V at $x = 0$: by using the expression of V_{E1c}, α can be calculated as

$$\alpha = 1 - \frac{2V_{E1c}}{V_{CC}} \tag{14}$$

and V_{out} can be expressed by combining (14) and (9) as:

$$V_{out} = x\frac{V_{CC}}{2}\frac{(V_{CC} - 2V_{E1c})}{(V_{CC} - V_{E1c}(1-x))} \tag{15}$$

x can be easily found as

$$x = \frac{V_{out}}{\frac{V_{CC}}{2}}\frac{(V_{CC} - V_{E1c})}{(V_{CC} - 2V_{E1c}) - V_{E1c}V_{out}} \tag{16}$$

and $x_{est,lin}$—the estimation of x by using the linearization expression of V_{out}—can be easily found as

$$x_{est,lin} = \frac{V_{out}}{\frac{V_{CC}}{2}}\frac{(V_{CC} - V_{E1c})}{(V_{CC} - 2V_{E1c})} \tag{17}$$

2.2. Experimental setup

The proposed method was validated using an instrumented canti-

lever beam equipped with printed sensors (Fig. 4a). Four printed strain gauges were fabricated on a steel bar (300 mm x 40 mm x 2.5 mm) to validate simultaneously two half bridges. The details related to the design of the strain gauges and their fabrication process are reported in Section 2.3. As shown in Fig. 4b, the instrumented bar was fixed to one end and bent by applying a downward force F on its free end. The printed strain gauges R_1 and R_3, printed on the top of the bar (Fig. 4b), measure the tensile strain ε_L of the bar induced by the applied load F (Fig. 4c), in the area where the sensors are placed. Between R_1 and R_3 a commercial strain gauge of resistance R_{comm} was installed as reference sensor. The reference strain gauge (C2A-06-015LW-120, Micro-measurements) has a nominal resistance of $(120.00 \pm 0.72)\Omega$ and a gauge factor of (2.03 ± 0.4). The strain gauges of resistance R_2 and R_4, printed on the bottom on the bar, measure the compression strain $(-\varepsilon_L)$. The sensors were printed with their center grid at $L = 175$ mm.

To ensure proper constraint, the bar was fixed such that L_0 equal to 220 mm. The higher the applied downward force F, the higher the strain ε_L. Indeed, the elastic deflection δ of the bar under the load F is maximum at the free end and can be calculated as

$$\delta_{max} = \frac{F \cdot L_0^3}{3E \cdot I} \tag{18}$$

where E is the Young's modulus, and I is the moment of inertia of the cross-sectional area with respect to the z-axis.

For a rectangular bar,

$$\mathrm{I} = \frac{wh^3}{12} \tag{19}$$

where w and h are the width and the thickness of the cantilever, respectively.

By substituting the expression of I from (19) into (18) and rearranging the equation to solve for E,

$$E = \frac{F \cdot 4L_0^3}{\delta_{max} \cdot w \cdot h^3} \tag{20}$$

According to the flexural formula [31], when the bar is made of isotropic linear elastic material the strain ε_L at the sensor location can be written as

$$\varepsilon_L = \frac{\sigma}{E} = \frac{\frac{F \cdot L \frac{h}{2}}{I}}{E} = \frac{6F \cdot L}{E \cdot w \cdot h^2} \tag{21}$$

where σ is the bending stress in the sensor region. Since all sensors are placed at the same longitudinal distance from the point of force application, the strain measured by the commercial and printed gauges is expected to be the same.

Finally, starting from (3), the strain ε_L can also be derived from the fractional resistance change of the commercial strain gauge, x_{comm}, as

$$\varepsilon_L = \frac{x_{comm}}{K_{comm}} \tag{22}$$

where K_{comm} is the gauge factor of the commercial sensor.

The force F was applied at the free end of the cantilever by using a Mark-10 force test stand equipped with a 250 N load cell (Fig. 4c). The tensile machine provides transverse displacement with an accuracy of 0.05 mm and the force measurements with an accuracy of 0.25 N. A special bar was held by the upper chuck (directly connected to the load cell of the tensile system) to apply the force on the cantilever. The tensile system was operated in position control: the transverse displacement corresponded to the cantilever deflection, with 0 mm indicating initial contact and zero force. Two profiles for the transverse movement were used:

1. Profile #1 (Fig. 5a): the transverse was moved from 0 mm to h_{max} (downward and upward, respectively) continuously with the transverse speed of 6 mm/min. h_{max} was changed from 0 up to 10 mm with step 1 mm in the test for determining the elastic region of the bars. h_{max} was set to 3 mm to validate the proposed method.
2. Profile #2 (Fig. 5b): the transverse was moved from 0 mm to 3 mm (downward and upward, respectively) with step 0.2 mm every 14 s. The transverse speed was set to 6 mm/min to reach the next setpoint in less than 3 s.

The setup related to the electronic instrumentation is schematically depicted in Fig. 4d. The following high-performance instrumentation was adopted:

- An Agilent 33120A function generator was employed to provide two independent controllable DC outputs, with an accuracy of 2%. Each of these two DC outputs was connected to a voltage follower circuit, devoted to generating a proper V_{E1} and V_{E2}. The voltage follower circuits were designed to increase the output impedances of the function generator.
- One GW Instek GPP-3650 triple-channel programmable DC power supply was used to provide V_{CC} (admissible values: 1.8 V, 2.5 V, 3.3 V and 5 V) and the dual power supply (±15 V) for the two voltage follower circuits.
- Five Keysight 34465A 6½-digit multimeters were used to measure $V_{CC}, V_{E1A}, V_{E1B}, V_{b2} - V_{b1A}$ and , $V_{b2} - V_{b1B}$. The declared accuracy (coverage factor = 1) is less than 7 μV in the range 0 mV to 200 mV, less than 35 μV in the range 200 mV to 1 V and less than 63 μV in the range 2 V to 3.3 V.
- An additional Six Keysight 34465A 6½-digit multimeter was used to measure R_{comm} during the tests, with an accuracy (coverage factor = 2) lower than 10.8 mΩ in R_{comm} range, and to measure the initial resistance of the printed sensors, accuracy (coverage factor = 2) between 8.6 mΩ and 15 mΩ in sensor range.

Two commercial resistors of $(100.0 \pm 0.1)\Omega$ were used as R_0.
Each test was performed according to the following two phases:

1) V_{E1A} and V_{E1B} were modified until V_{b1A}, and V_{b1B} were equal to $\frac{V_{CC}}{2}$.
2) The tensile system was controlled by using the proper profile, repeated six times, and the measurements from the multimeters and the tensile system were taken at the same time.

The movements of the tensile system and the acquisition of the data from the instrumentation were controlled automatically via USB by using a custom-made Virtual Instrument (developed in the LabVIEW environment). Measurements were synchronized and recorded every 0.3 s.

All tests were performed at room temperature (25 °C ± 1 °C), and the instrumented bars were tested 1 h after connecting and powering the experimental setup to reach good stability of the sensor output due to the influence of the temperature. When a current flows in the sensor, the temperature increases, and therefore the resistance increases; the heat dissipation is limited by the insulating layer. Before thermal equilibrium is reached, the resistance gradually decreases due to heat exchange with the environment. This equilibrium is reached after a certain time due to settling time of the instrumentation and the high volume of the steel bar.

2.3. Strain gauges fabrication

The strain gauges were designed using a 2D Computer-Aided Design environment. An example of the printed strain gauge is shown in Fig. 6a. The gauge sensor has a length (l) of 17.5 mm, a width (w) of 7.35 mm, and a spacing (s) of 0.35 mm. The expected width of the lines is 150 μm. Scanning electron microscope analysis performed with Phenom XL G2 Desktop SEM revealed several defects (Fig. 6b), such as holes or over-spray, which can explain the high tolerance in electrical resistance

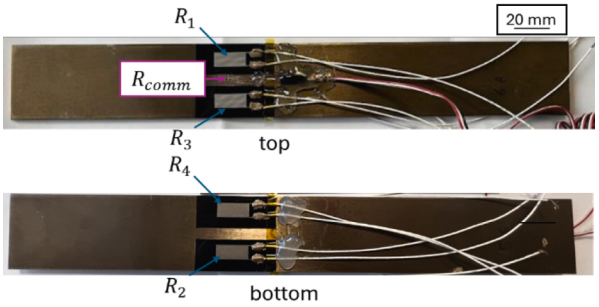

(a)

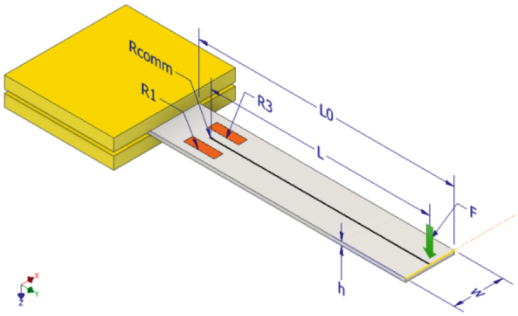

(b)

(c)

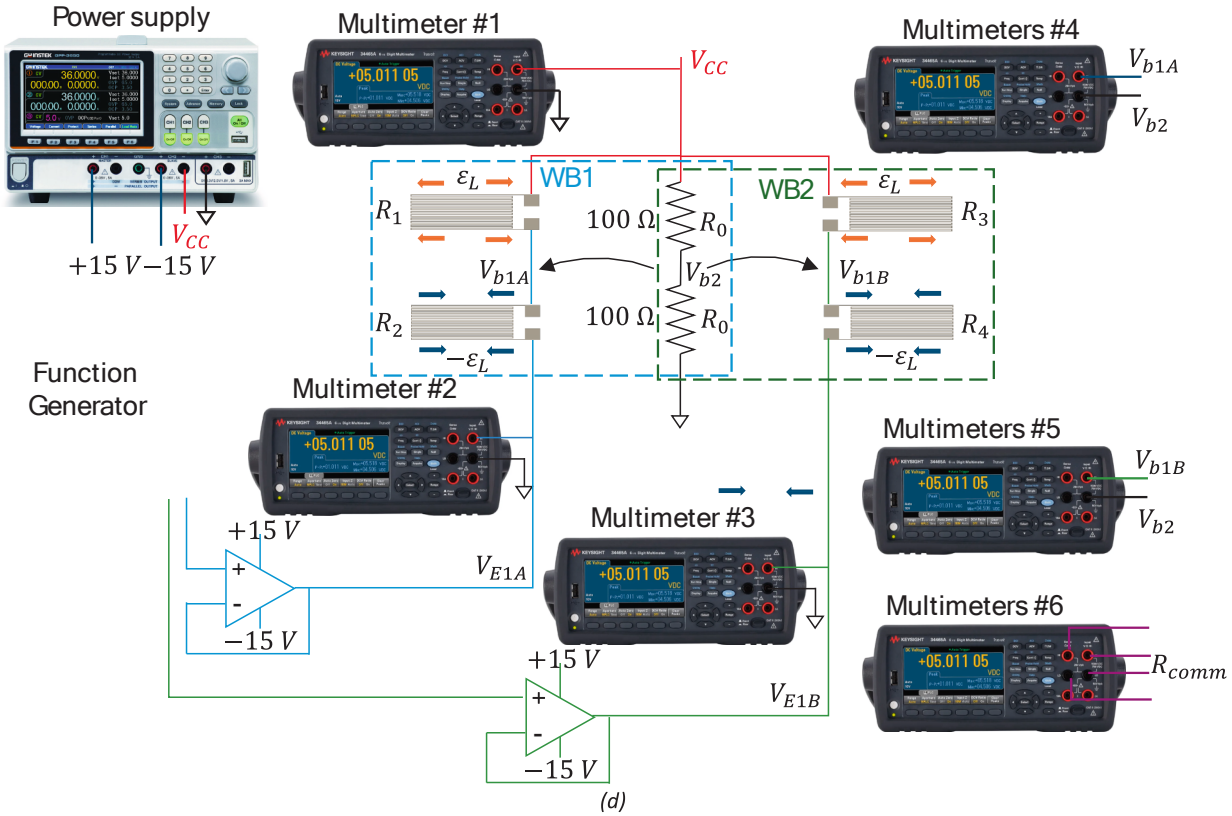

(d)

Fig. 4. (a) Device under test: top view and bottom view of the printed cantilever. The commercial strain gauge (R_{comm}) is used as a reference, R_1, R_2, R_3 and R_4 are the printed sensors of a printed bar. (b) Schematic representation of the tensile setup. (c) Tensile setup. (d) Schematic block diagram of the measurement setup for the device under test. R_{comm} of the commercial strain gauge is measured by using the four-probe method. The power supply provides the power for the WBs and the conditioning circuits for interfacing the function generator with V_{E1A} and V_{E1B}. While ε_L is the strain induced by F exerted by the tensile system. R_0 represents the resistance of the two commercial resistors used as the second branch of the WB.

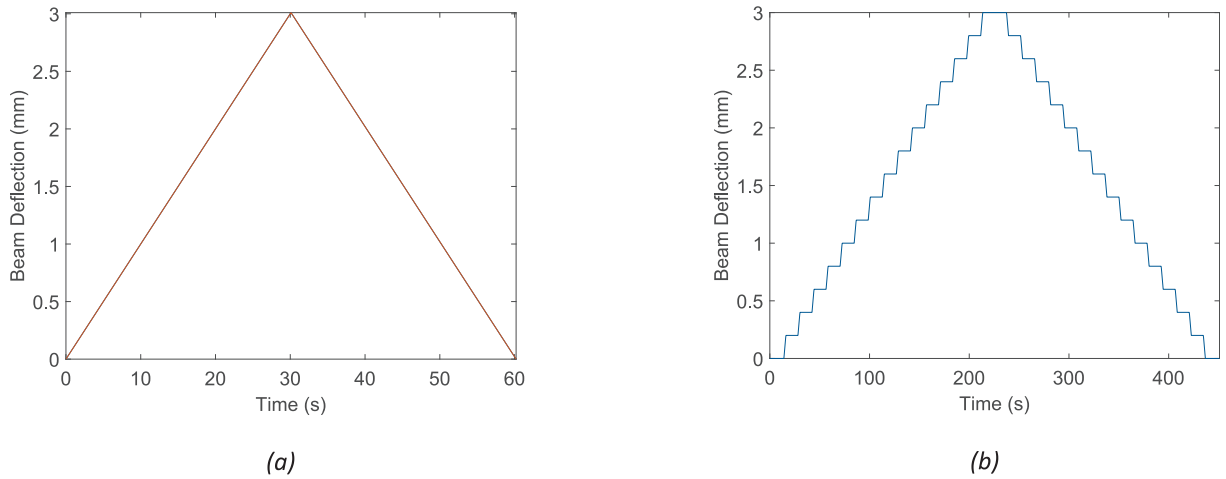

Fig. 5. Representation of (a) Profile #1 in the case ofh_{max} = 3 mm and (b) Profile #2 for controlling the position and the applied force at the free end of the cantilever.

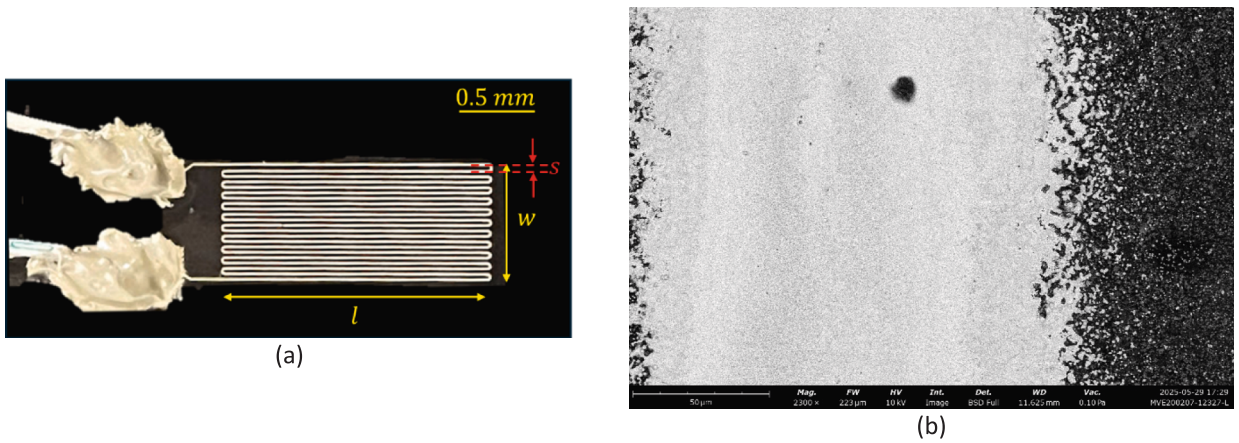

Fig. 6. (a) One example of the printed strain gauge; (b) Scanning Electron Microscope (SEM) image of a printed sensor.

among the sensors.

The fabrication process consisted of the following steps:

a) *Deposition of the Insulating Layer*: to electrically isolate the conductive steel bar, a thin insulating layer (Elcron ALCROLUX 600) was deposited. The bar was masked to expose four regions of dimensions $l \times h$, corresponding to the sensor locations. The ink was deposited by using an airbrush and cured at 150 °C for 15 min. To ensure complete insulation, the entire process was repeated twice, followed by oven curing at 200 °C for 60 min.

b) *Fabrication of Strain Gauges Using Aerosol Jet Printing*: strain gauges were printed using an aerosol jet printing system (Optomec AJ-300). A 3D CAD model was prepared to guide the movement of the print head and platen. Based on the ink viscosity (30–45 cP), a pneumatic collision atomizer was used to generate an aerosol mist from the silver ink (Utdot). The thinner provided by the ink manufacturer was introduced via bubbler to aid in the atomization process. The ink was stirred and atomized by nitrogen carrier gas, then directed to the print head. Excess gas was removed using a virtual impactor, which also controlled droplet size (1–5 μm). A nitrogen sheath gas focused the aerosol beam, reducing to a tenth of the nozzle diameter, and preventing nozzle clogging. The substrate was mounted on a temperature-controlled platen set to 80 °C to promote solvent evaporation. Printing parameters included: 750 μm nozzle diameter, 2 mm/s printing speed, and 4 mm nozzle-to-substrate distance. Gas flow rates were 590 sccm (carrier gas), 540 sccm (exhaust gas), and 1000 sccm (sheath gas). The deposition process was repeated twice to ensure adequate resistance, matching the reference strain gauge.

c) *Sintering Process*: printed metal bars were heated at 300 °C for 2 h to remove solvents and additives, ensuring proper adhesion and conductivity.

d) *Electrical Contacting*: electrical connections between the printed strain gauges and external wiring were established using conductive and adhesive epoxy (EPO-TEK® H20E) manually applied to the pads and cured at 150 °C under controlled humidity for 1 h. High-temperature wires (15 cm long) with a temperature rating up to 200 °C were used to ensure thermal stability.

e) *Protective Coating*: each strain gauge was encapsulated with a transparent protective and flexible silicone coating (RS 494–714 m), manually sprayed. After 2 h at 20 °C, the bar was cured at 90 °C for 22 h, as recommended. This prevents oxidation of the conductive tracks.

3. Results and discussion

To experimentally validate the method, six half-bridges with different initial resistance ratio (αvalues) and supply voltages (V_{CC}) were tested.

3.1. Mechanical characteristics

The mechanical properties of the steel bars, especially Young's

module and elastic region, were experimentally determined prior to the method validation. The elastic region was identified by using Profile #1 on a bare bar, varying h_{max}. Results showed that a maximum load of 20 N maintained the cantilever within the elastic region, corresponding to a maximum deflection of 5 mm. To ensure operation within a safe range, h_{max} was set to 3 mm for the subsequent tests. For $h_{max} = 3mm$, the relationship between the deflection (h) and the applied load (F) was found to be linear (R-squared = 0.999) and repeatable, as shown in Fig. 7. These results were obtained by using Profile #2, repeated 20 times. All measurements fell within the accuracy range of the tensile system, represented by the bars around the mean value. The Young's modulus (E) of the instrumented bar was estimated to be (260.73 ± 0.67) GPa, with 95% confidence level (degree of freedom = 638). Using the slope of the least squares regression line (LSRL), $m_{F/\delta}$ and (20), E was calculated as

$$E = m_{F/\delta}\frac{L_0^3}{3 \cdot I} \tag{23}$$

The standard uncertainty was derived by multiplying the square root of the experimental variance of the slope by $\frac{L_0^3}{3 \cdot I}$, assuming negligible uncertainty in geometrical quantities. Equivalent results were obtained for the other two bars, and hysteresis was negligible across all the repetitions, as expected.

3.2. Sensor characteristics

Fig. 8 shows the fractional relative change in resistance of the commercial strain gauge as a function of strain. Strain values on the x-axis were calculated from bar deflection measurements provided by the tensile system using (20). The gauge factor, determined via least square regression method, was 2.05, consistent with the declared specifications (2.03 ± 0.04). Measurements were obtained by using Profile #2. The maximum absolute deviation (MAD), defined as the maximum difference between the measurements and the mean value at each strain level, was less than 1 mΩ, within the accuracy of the multimeter.

Printed sensors were also evaluated using the 4-wire ohms function to determine their gauge factors. As shown in Fig. 9, x of the printed sensors of bar #1 linearly changes with tensile strain (R_1 and R_3) and

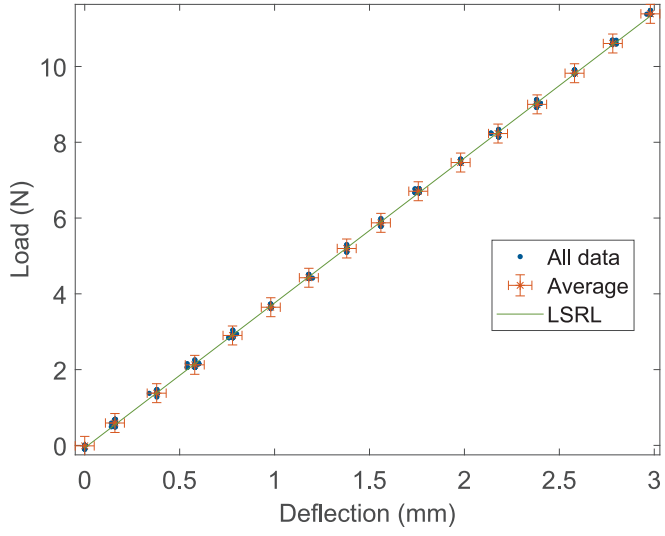

Fig. 7. Maximum bar deflection and the load measured by the tensile system. The results are obtained by using Profile #2, repeated 20 times. The 16 blue squares represent the 640 measurements (32 travel positions for 20 repetitions), and the red stars represent the 32-mean value (the error bars represent the declared accuracy of the tensile machine). The green line is the least squares regression line. (For interpretation of the references to colour in this figure legend, the reader is referred to the web version of this article.)

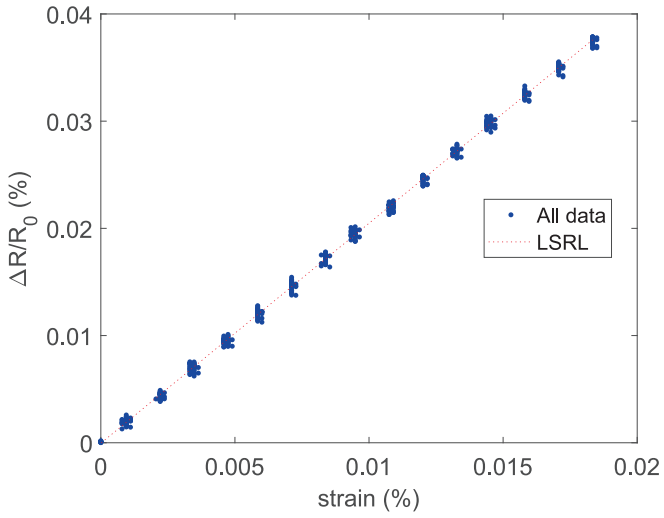

Fig. 8. Fractional relative change in the commercial strain gauge resistance (mounted on bar #1) and the strain of the bar at L = 175 mm, where the strain sensor is located. The dots represent the measurements obtained by using Profile #2, with 20 repetitions, and the dotted line is the LSRL found considering all the data.

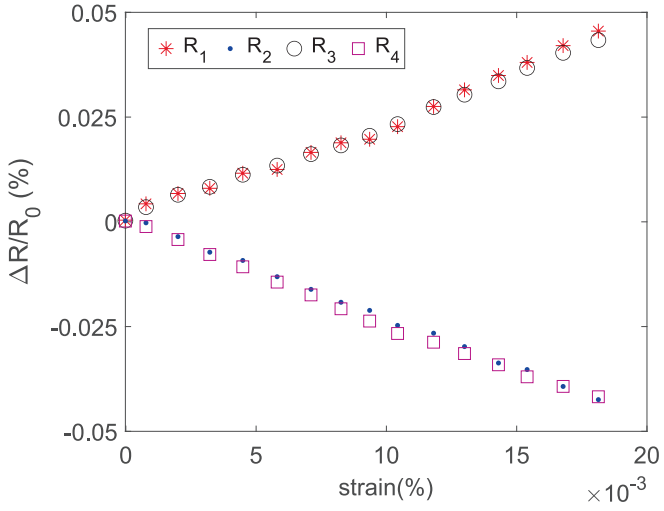

Fig. 9. Fractional relative change in the printed strain gauges (fabricated on bar #1). The stars are the measurements taken for increasing force and the triangles for decreasing force (Profile #2).

compressive strain (R_2 and R_4), as expected. Strain was calculated using (22), based on the strain gauge response. The resulting gauge factors were consistent across sensors despite differing nominal resistances (α ranging from 0.42 to 1.88), as shown in Table I. MAD values ranged from 0.2 to 0.6 mΩ, similar to the commercial strain gauge, and consistent across all three instrumented bars.

Table I
Resistance and gauge factor of the sensors on the instrumented bars.

	Bar #1		Bar #2		Bar #3	
	$R_0(\Omega)$	K	$R_0(\Omega)$	K	$R_0(\Omega)$	K
R_1	139.581	2.40	67.789	3.05	75.169	2.77
R_2	262.300	2.38	123.229	3.10	79.297	2.80
R_3	127.497	2.31	67.402	2.97	76.399	2.79
R_4	143.925	2.38	157.651	3.02	75.707	2.79
R_{comm}	120.373	2.05	120.720	2.06	120.163	2.04

3.3. Validation of the balancing method on a half WB configuration

Results for half WB1 of bar #1, using Profile #2, aligned with the theoretical predictions in Section 2.1. Measured and expected α were 1.881 and 1.879, respectively, while V_{CC} was 3.25345 (0.00001) V and V_{E1c} was 1.366230 (0.000003) V (in the brackets the experimental standard deviation calculated on 1600 samples). The balancing procedure led to an initial average offset on V_{out} of 21 μV, attributed to the accuracy of the experimental setup, in particular the resolution of V_{E1}. Fig. 10 presents the responses of the commercial strain gauge and the proposed circuit. For each strain level, voltage and resistance measurements were averaged over the last 30 samples.

Fig. 11 shows the averaged strain and V_{out} measurements. Standard deviations were omitted because they were smaller than the symbol size. The relationship between the strain (measured by the commercial strain gauge) and V_{out} was linear, with a slope matching the theoretical value $\frac{\alpha}{(1+\alpha)}V_{CC}$, which was 5.075 V/mm/mm. MAD was less than 0.05 mV and could be further reduced by subtracting the initial V_{out} offset.

Similar considerations can be extended to the resulting relationship between the strain found starting from the commercial sensor response and x_{est} calculated from the V_{out} response. As shown in Fig. 12, the trend is the same as represented in Fig. 11, with a different scale on the y-axis. The fitting line has a slope of 2.389, between the gauge factor of R_1 and R_2. A two-point calibration procedure may suffice due to the quasi-linear bridge response. Linearity error was 5%/FS, with FS = 0.0184% (the maximum investigated strain). The offset of the fitted line, i.e., the value of the estimated x for strain = 0%, was influenced by the resolution of the reference voltage bridge, which affects the bridge balance, and α estimation. Negligible differences were observed between x_{est} calculated by using (12) or (16) and $x_{est,lin}$ calculated by using (13) or (17).

A similar trend was observed by changing the value of V_{CC}, as shown in Fig. 13. Three values of V_{ref} were chosen: 1.767600 (0.000006) V, 2.48492 (0.00001) V, and 3.25369 (0.00001) V, and six repetitions of Profile #2 were performed for each level of V_{ref}. The linearity was preserved, as well as the linearity error, which was less than 5%/FS. For example, in the case of half WB1 of bar #1, the sensitivity of the circuit increased according to V_{CC}, from 2.758 V/(mm/mm) to 5.077 V/(mm/mm), as expected, while the MAD on the estimated strain did not change. The error bars represent the maximum deviation of each repetition for the same V_{CC} value, considering all measurements taken both in the loading and unloading phase. The maximum deviation is always less than 2.8%/FS (where FS is the mean V_{out} at the maximum strain), regardless of the V_{CC} value.

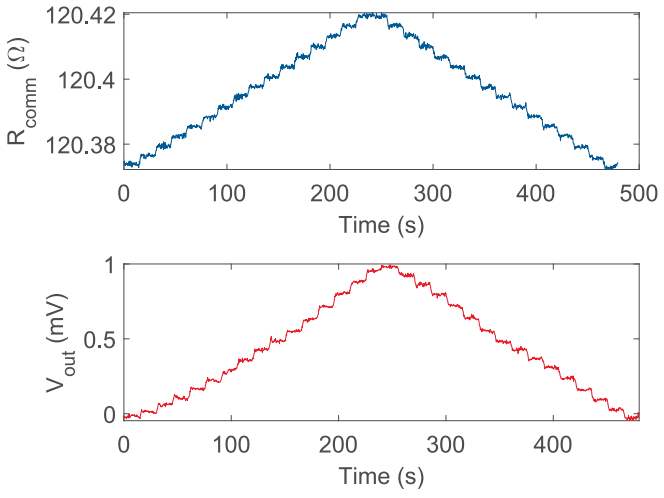

Fig. 10. Response of the strain gauge in terms of resistance and of the proposed circuit in terms of V_{out} when half WB1 of bar#1 was tested with Profile #2. ($V_{ref} = 3.25V$ and $\delta_{max} = 3mm$).

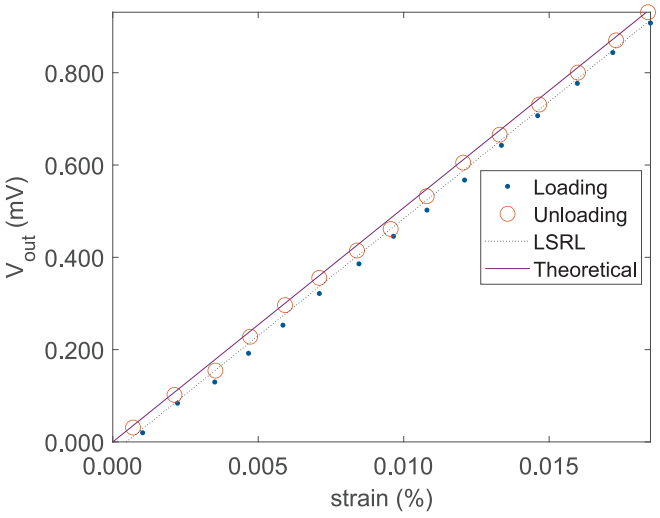

Fig. 11. Mean V_{out} (calculated on the last 20 samples before changing the next strain level) according to the strain level (measured by the commercial strain gauge) in the loading (star symbols) and unloading (circle symbols) of half WB1 of bar#1. The results were obtained by using Profile #2 for the tensile machine control and $V_{ref} = 3.253454$ V. The theoretical V_{out} (solid line) was calculated by using (15) is shown for comparison, while LSRL (dotted line) is the fitting line calculated with the least-squares method.

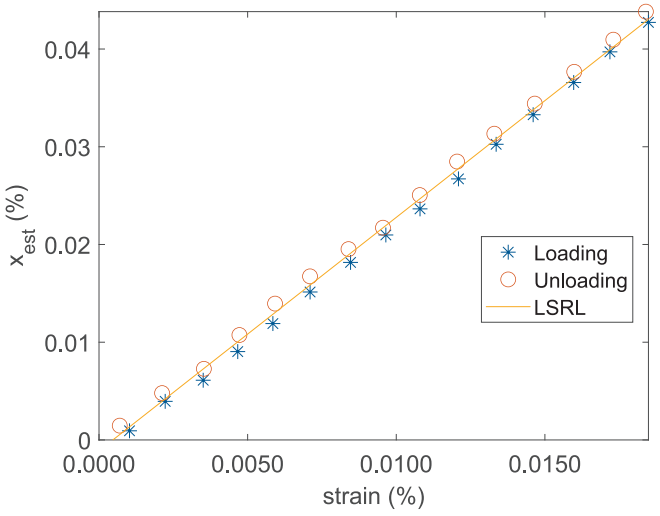

Fig. 12. x_{est} calculated from the mean V_{out} according to the strain level (measured by the commercial strain gauge) in the loading (star symbols) and unloading (circle symbols) of half WB1 of bar#1. The results were obtained by using Profile #2 for the tensile machine control and $V_{CC} = 3.253454$ V. The yellow line is the fitting line calculated with the least-squares method. (For interpretation of the references to colour in this figure legend, the reader is referred to the web version of this article.)

Comparable results were obtained for the other half WBs of the printed instrumented bars, as shown in Fig. 14. In this figure, the results are related to the tests with average V_{CC} equal to 3.25369 V, but the results are similar for the other values of V_{CC}, as already proved for bar#1. The slope depends on α, which differs according to the tested bars. As found for half WB1 of bar#1, V_{out} can be fitted with a LSRL, which is in accordance with the theoretical one. The linearity error, the hysteresis, and repeatability are the same or better than those obtained for bar#1. For example, the linearity error is 2.6%/FS (with FS equal to 0.480 mV) for WB2 of bar #3 (worst case). By calculating x from V_{out} and approximating to a first-order regression, the sensitivity with

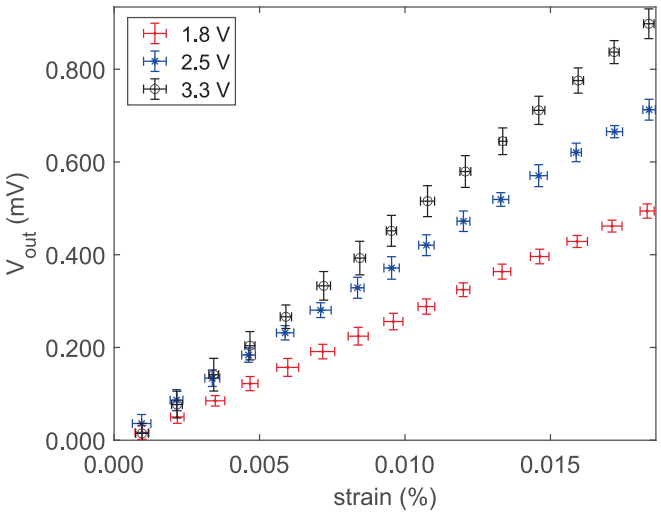

Fig. 13. Response of the bar#1 in terms of V_{out} according to the strain measured by the commercial strain gauge in six repetitions and at different V_{CC} values. Dots are the average values, and the bars are the maximum deviation between the mean value and the measurements for each strain level. The results were obtained by using Profile #2 for the tensile machine control.

respect to the applied strain is 2.39 (WB1 of bar #1), 3.07 (WB1 of bar #2), 2.79 (WB1 of bar #3), 2.34 (WB2 of bar #1), 2.99 (WB2 of bar #2), and 2.79 (WB2 of bar #3).

An additional test was performed before allowing the sensor resistance to stabilize. Indeed, in this condition, while the resistance of the commercial stain gauge was constant at strain = 0%, the resistance of the printed sensors was characterized by a drift over time. One of the main advantages of the traditional half WB configuration is the ability to compensate for the sensor drift when it is equal for all the sensors. For this reason, a first cyclic test (obtained by using Profile #1 three times) was performed on bar #3 by measuring the resistance of the commercial sensor and the two sensors. As shown in Fig. 15, the commercial sensor resistance changes according to strain induced by the tensile system with good repeatability. Both R_1 and R_2 respond according to the strain in addition to a drift over time. Considering R_1 and R_2 at strain = 0%, the resistances at the end of the third cycle decreased by 0.37%, with respect to their initial values. In Fig. 15b and Fig. 15c, the consequences of this drift are more evident: the fractional resistance change is strongly different in each cycle, and the absolute maximum value decreases in the case of R_1 (under tensile strain) and increases in the case of R_2 (under compressive strain) after three cycles.

The test was repeated using the proposed experimental setup, with an average V_{CC} equal to 3.25369 V. The results shown in Fig. 16 show that the resistance drift does not significantly affect V_{out}, and does not affect the repeatability and the hysteresis of the calibration curve, as shown in Fig. 16b and Fig. 16c.

4. Conclusion

The proposed voltage-based balancing method provides an effective and scalable solution for compensating resistance mismatches in printed Wheatstone bridges, eliminating the need for manual trimming or expensive analog circuitry. Compared to existing methods, it effeciently regulates half Wheatstone bridges, ensuring accurate compensation of printed strain-gauge tolerance with minimal instrumentation. The experimental validation using printed strain gauges on a flexible cantilever beam demonstrated the method's capability to handle large tolerance spreads. Using benchtop, the initial offset due to the high mismatch of sensors (with α from 0.42 to 1.88) was reduced to less than 21 μV, with linearity preserved (less than 5%/FS) and output stability mantained even in presence of resistance drift. The method is effective for resistors with significantly different values but comparable sensitivity. This method offers a practical solution for improving measurement accuracy in printed sensor systems, making it ideal for applications in wearable electronics, soft robotics, structural health monitoring, and disposable or conformal sensor platforms, where simple integration and adaptability are essential. Its implementation using a single controllable reference voltage makes it compatible with scalable and automated production processes, and inherently suitable for integration with printed and flexible electronics. Furthermore, the proposed technique can be readily adapted for automatic calibration using standard commercial off-the-shelf components. For example, a microcontroller equipped with a digital-to-analog converter (DAC) can directly generate and adjust the reference voltage, enabling fully automated bridge balancing without additional complex analog circuitry. Future works could focus on optimizing the front-end circuitry to enhance resolution, accuracy, and balancing performance.

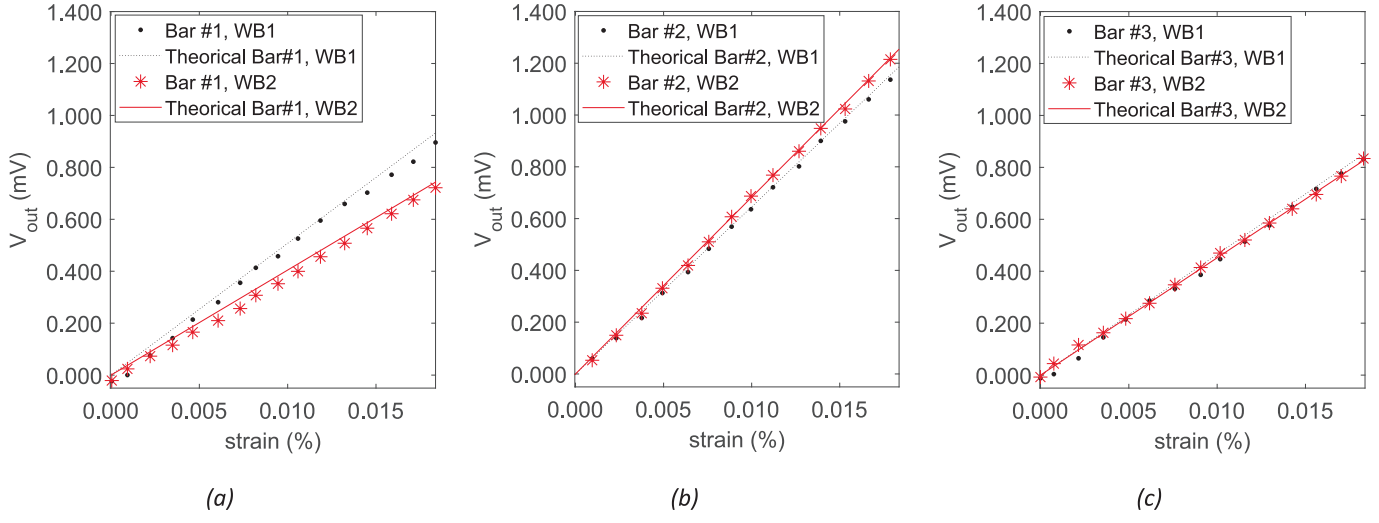

Fig. 14. Mean V_{out} (calculated on the last 20 samples before changing the next strain level) according to the strain level (measured by the commercial strain gauge) of the instrumented (a) bar#1, (b) bar#2, and (c) bar #3 (V_{CC} = 3.25V). The results were obtained by using Profile #2 for the tensile machine control and V_{CC} = 3.253454 V. The theorical V_{out} (line) was calculated by using (9) for comparison.

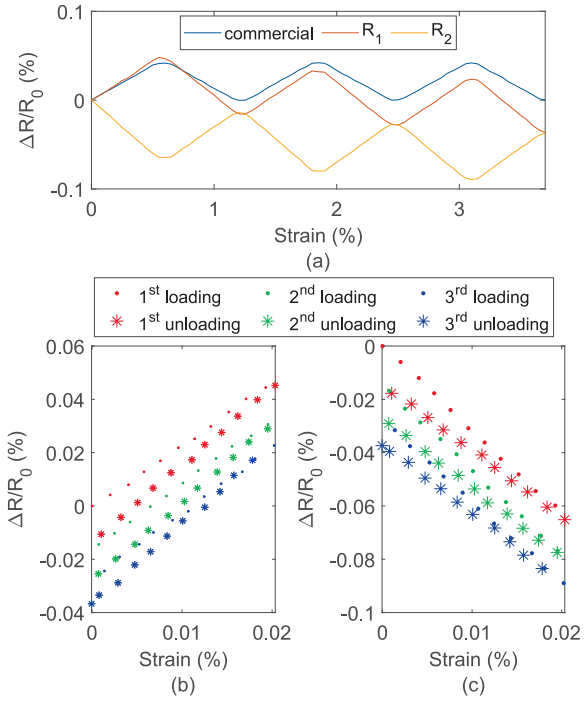

Fig. 15. (a) Commercial and printed sensor response over time, (b) factional resistance change of (b) R_1 (c) and R_2 according to the strain measured by the commercial strain, when the Profile #1 is used to deflect the bar #3.

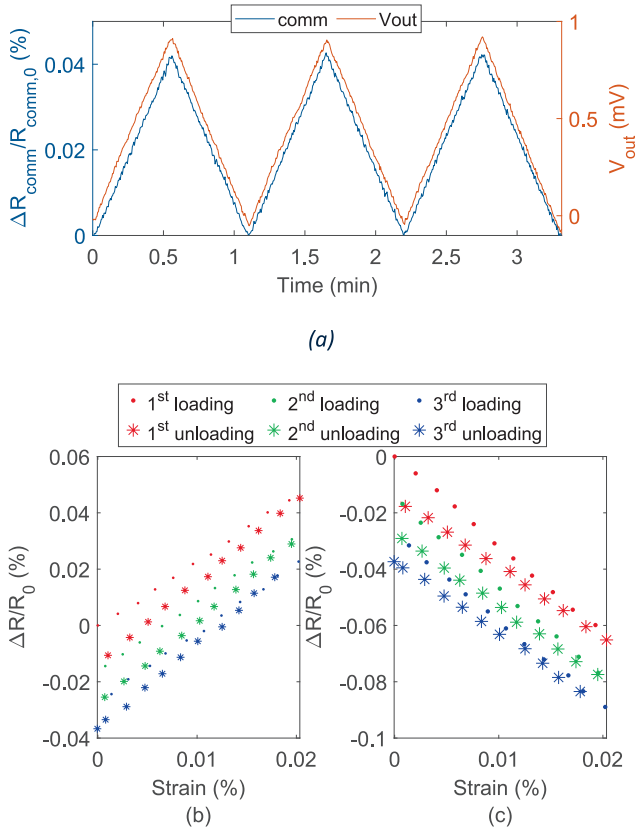

Fig. 16. (a) Commercial and V_{out} of the WB1 of bar#3 circuit over time, (b) V_{out} and (c) estimated overall fractional resistance change of the printed sensors, when the Profile #1 is used to deflect bar #3.

CRediT authorship contribution statement

Michela Borghetti: Writing – review & editing, Writing – original draft, Visualization, Validation, Software, Resources, Methodology, Investigation, Formal analysis, Data curation, Conceptualization. **Emilio Sardini:** Supervision, Project administration, Funding acquisition, Conceptualization. **Mauro Serpelloni:** Writing – original draft, Methodology, Investigation, Conceptualization.

Declaration of competing interest

The authors declare that they have no known competing financial interests or personal relationships that could have appeared to influence the work reported in this paper.

Acknowledgment

This study was carried out within the MICS (Made in Italy – Circular and Sustainable) Extended Partnership and received funding from the European Union Next-GenerationEU (PIANO NAZIONALE DI RIPRESA E RESILIENZA (PNRR) – MISSIONE 4 COMPONENTE 2, INVESTIMENTO 1.3 – D.D. 1551.11-10-2022, PE00000004). This manuscript reflects only the authors' views and opinions, neither the European Union nor the European Commission can be considered responsible for them.

Data availability

Data will be made available on request.

References

[1] A. De Marcellis, G. Ferri, Resistive, Capacitive and temperature sensor interfacing overview, in: Analog circuits and systems for voltage-mode and current-mode sensor interfacing applications, Springer, 2011: pp. 37–74. https://link.springer.com/chapter/10.1007/978-90-481-9828-3_2.

[2] L. Angrisani, P. Arpaia, M. D'Arco, E. De Benedetto, A. Esposito, M. Imbó, A. Tedesco, Measurement sustainability: a first methodological step for its modeling and assessment, Measurement 209 (2023) 112539, https://doi.org/10.1016/j.measurement.2023.112539.

[3] H.-S. Cha, S.-H. Hwang, D.-H. Kim, H.-I. Kwon, S.-H. Song, Wheatstone bridge based offset cancelling method utilizing a JFET as a voltage-controlled resistor, Measurement 186 (2021) 110128, https://doi.org/10.1016/j.measurement.2021.110128.

[4] S. Pan, K.A.A. Makinwa, Wheatstone Bridge–Based Temperature Sensors, in: Resistor-Based Temperature Sensors in CMOS Technology, Springer, 2022: pp. 67–106. https://link.springer.com/chapter/10.1007/978-3-030-95284-6_4.

[5] D.M. Stefănescu, Handbook of force transducers: principles and components, Springer (2020), https://doi.org/10.1007/978-3-642-18296-9.

[6] C.-H. Tan, Y.-C. Lin, Y.-C. Chou, others, a high-sensitivity AlGaN/GaN pressure sensor based on a Wheatstone bridge configuration, AIP Adv. 8 (2018) 55015, https://doi.org/10.1063/1.4996257.

[7] M. Tanyeri, M. Ranka, N. Sittipolkul, C.M. Schroeder, Microfluidic Wheatstone bridge for rapid sample analysis, Lab Chip 11 (2011) 4181–4186, https://doi.org/10.1039/C1LC20604D.

[8] M.J. Hossain, B.T. Tabatabaei, M. Kiki, J.-W. Choi, Additive manufacturing of sensors: a comprehensive review, Int. J. Precis. Eng. Manufact.-Green Technol. 12 (2025) 277–300, https://doi.org/10.1007/s40684-024-00629-5.

[9] M. Georgas, others, Temperature sensors by inkjet printing compatible with flexible substrates: a review, IEEE Sens J 23 (2023) 21–33. Doi: 10.1109/JSEN.2022.3213072.

[10] C. Bali, A. Brandlmaier, A. Ganster, O. Raab, J. Zapf, A. Hübler, Fully inkjet-printed flexible temperature sensors based on carbon and PEDOT:PSS1, Mater. Today Proc. 3 (2016) 739–745, https://doi.org/10.1016/j.matpr.2016.02.005.

[11] B. Weng, A. Morrin, R. Shepherd, K. Crowley, A.J. Killard, P.C. Innis, G.G. Wallace, Wholly printed polypyrrole nanoparticle-based biosensors on flexible substrate, J. Mater. Chem. B 2 (2014) 793–799, https://doi.org/10.1039/c3tb21378a.

[12] A. Hobbie, J. Smith, K. Lee, et al., Aerosol jet printing of conformal sensors on flexible and curved substrates, npj Flexible Electron. 8 (2024) 12, https://doi.org/10.1038/s41528-024-00340-0.

[13] M. Saeidi-Javash, et al., All-printed MXene-Graphene nanosheet-based bimodal sensors for simultaneous strain and temperature sensing, ACS Appl. Electron. Mater. (2021), https://doi.org/10.1021/acsaelm.1c00218.

[14] E. Bessac, et al., Printed temperature sensors on paper with aerosol jet printing technology, IEEE International Conference on Flexible and Printable Sensors and Systems (FLEPS) (2024), https://doi.org/10.1109/FLEPS61194.2024.10603487.

[15] Y.P.Q. Yi, Y. Li, Inkjet conductive inks for printing textile materials and applications ? J. Fiber Bioeng. Inf. 12 (2019) https://doi.org/10.3993/JFBIM00310.
[16] Y. Liu, Y. Zhu, 3D-Printed SoftWearable electronics: techniques, materials, and applications, in: Additive Manufacturing Materials, Functionalities and Applications, 2022. Doi: 10.1007/978-3-031-04721-3_1.
[17] Y. Han, W.F. Lu, Structural design of wearable electronics suitable for highly-stretched joint areas, Smart Mater. Struct. 27 (2018) 105042, https://doi.org/10.1088/1361-665X/aadf05.
[18] A. Zitoun, D. Fakis, N. Jayasree, S. Omairey, F. Oikonomidis, Z. Stoeva, M. Kazilas, Graphene-based strain sensing in composites for structural and health monitoring applications, SN Appl. Sci. 4 (2022) 58, https://doi.org/10.1007/s42452-022-04940-1.
[19] M. Borghetti, et al., Aerosol jet printed and photonic cured paper-based ammonia sensor for food smart packaging, IEEE Trans. Instrum. Meas. 71 (2022), https://doi.org/10.1109/TIM.2022.3161695.
[20] M. Borghetti, O. Casas, E. Sardini, M. Serpelloni, Novel method for balancing full wheatstone bridge for high-tolerance resistive sensors, IEEE Trans. Instrum. Meas. (2025), https://doi.org/10.1109/TIM.2025.3586341.
[21] W. Zhi-juan, Y. Xiao-dong, S. Yuan, Z. Xiao-bin, A software method to improve resistance measure precision of laser trimming system, in: Second International Workshop on Education Technology and Computer Science 2010 (2010) 586–589, https://doi.org/10.1109/ETCS.2010.221.
[22] Y. Zhang, et al., Design and optimization of wheatstone bridge adjustment circuit for resistive sensors, IEEE Sens. J. 23 (2023) 14330–14338, https://doi.org/10.1109/JSEN.2023.3274927.
[23] A. Dutta, T.K. Bhattacharyya, Low Offset, Low Noise, Variable Gain Interfacing Circuit for MEMS Based, Wheatstone Bridge Type, Resistive Smart Sensor, in: IEEE International Conference on VLSI Design, 2011: pp. 322–327. Doi: 10.1109/VLSID.2011.39.
[24] Y. Kwon, H. Kim, J. Kim, K. Han, D. You, H. Heo, D.D. Cho, H. Ko, Fully differential chopper-stabilized multipath current-feedback instrumentation amplifier with R-2R DAC offset adjustment for resistive bridge sensors, Appl. Sci. 10 (2019) 63, https://doi.org/10.3390/app10010063.
[25] A. De Marcellis, et al., Current-based measurement technique for high sensitivity detection of resistive bridges with external balancing through control voltages, IEEE Sens. J. 17 (2017) 404–411, https://doi.org/10.1109/JSEN.2016.2627640.
[26] A. De Marcellis, G. Ferri, P. Mantenuto, A novel 6-decades fully-analog uncalibrated Wheatstone bridge-based resistive sensor interface, Sens. Actuat. B Chem. 189 (2013) 130–140, https://doi.org/10.1016/j.snb.2013.02.014.
[27] P. Mantenuto, A. De Marcellis, G. Ferri, Uncalibrated analog bridge-based interface for wide-range resistive sensor estimation, IEEE Sens. J. 12 (2012) 1413–1414, https://doi.org/10.1109/JSEN.2011.2172414.
[28] T.H. Nguyen, H.T. Pham, N.D. Khoa Tran, D.A. Wang, Design and characterization of a compliant six axis force/torque sensor with low cross-axis sensitivity, Measurement 252 (2025) 117348. Doi: 10.1016/J.MEASUREMENT.2025.117348.
[29] M. Borghetti, M. Serpelloni, E. Sardini, S. Pandini, Mechanical behavior of strain sensors based on PEDOT:PSS and silver nanoparticles inks deposited on polymer substrate by inkjet printing, Sens. Actuat. A Phys. 243 (2016) 71–80, https://doi.org/10.1016/j.sna.2016.03.021.
[30] M. Borghetti, M. Serpelloni, E. Sardini, Printed strain gauge on 3D and low-melting point plastic surface by aerosol jet printing and photonic curing, Sensors (Switzerland) 19 (2019), https://doi.org/10.3390/s19194220.
[31] A.C. Mitra, A. Jagtap, S. Kachare, Development and validation of experimental setup for flexural formula of cantilever beam using NI-LabVIEW, Mater. Today Proc. 5 (2018) 20326–20335, https://doi.org/10.1016/j.matpr.2018.06.407.